

Time Developing Flow in a Lid Driven Cavity

AME 531 - Numerical Methods in Fluid Mechanics and Heat Transfer

Theo Altneu

University of Arizona

September 16, 2025

Abstract

This study investigates the transient development of incompressible two-dimensional flow inside a square lid-driven cavity using the Marker and Cell (MAC) method on a staggered grid. The governing equations are solved using the explicit MAC method, coupled with a pressure correction step obtained by solving a Poisson equation. The objectives are to validate the solver against established benchmark data for both top-driven and antiparallel cavity flows, to systematically study the effects of Reynolds number on flow structure evolution, and to investigate the impacts of timestep size and grid resolution on numerical accuracy and stability. The results confirm that the MAC solver reliably captures key flow structures such as primary and secondary vortices, boundary layers, and symmetric velocity profiles. The Reynolds number study shows a clear transition from viscous to inertia-dominated regimes, with sharper gradients and thinner boundary layers and increasing secondary vortex strength as Reynolds number increases.

1 Introduction

The lid-driven cavity flow is a fundamental benchmark problem in computational fluid dynamics (CFD) and fluid mechanics due to its simple geometry yet rich and complex flow behavior. It involves the motion of a viscous incompressible fluid within a square cavity, driven solely by the tangential motion of one or more walls, while the remaining walls remain stationary. Despite its geometric simplicity, the flow features include primary recirculating vortices, secondary corner vortices, boundary layer formation, and sharp velocity gradients, all of which make it an ideal testbed for validating numerical methods. Numerous studies have investigated this problem, notably the work by Ghia et al. (1982) [1], which provided highly accurate benchmark solutions for steady incompressible flow at various Reynolds numbers. Later studies, such as Perumal and Dass (2008) [2], extended the analysis to two-sided lid-driven cavities using alternative methods like the lattice Boltzmann method. The lid-driven cavity thus remains a classical test case for evaluating both the accuracy and stability of numerical solvers designed for incompressible Navier-Stokes equations. In this project, the transient development of incompressible two-dimensional flow inside a lid-driven cavity is investigated for two distinct boundary motion cases: antiparallel top and bottom wall motion, and corner-driven motion where the top wall moves horizontally and the left wall moves vertically. The governing equations are solved using an explicit Marker and Cell (MAC) method implemented on a staggered grid, coupled with a pressure correction step obtained by solving a Poisson equation. The objectives are to validate the solver against established benchmark results, to systematically study the effects of Reynolds number on flow structure evolution, and to investigate the impacts of timestep size and grid resolution on numerical accuracy and stability. Through these studies, this project aims to demonstrate the robustness and effectiveness of the MAC method for solving unsteady incompressible flow problems with moving boundary conditions.

2 Problem Formulation

The lid-driven cavity flow is a classical problem in computational fluid dynamics that involves a viscous incompressible fluid confined in a square cavity. The flow is set into motion by the tangential movement of the cavity's boundaries. In this study, the transient behavior of the flow field is investigated when the top wall moves with constant velocity and the bottom wall also moves with a specified magnitude and direction. For this paper, the bottom wall is given the same velocity as the top wall but acts in the opposite direction (antiparallel flow) as seen in Figure 1. A second case is also analyzed, where the top wall and the left wall is moving opposite as seen in Figure 2. For this paper, the left wall will be given the same velocity as the top wall and acts downwards. The goal is to understand how the flow evolves from an initial quiescent state to a fully developed configuration under the influence of boundary motion and viscous effects.

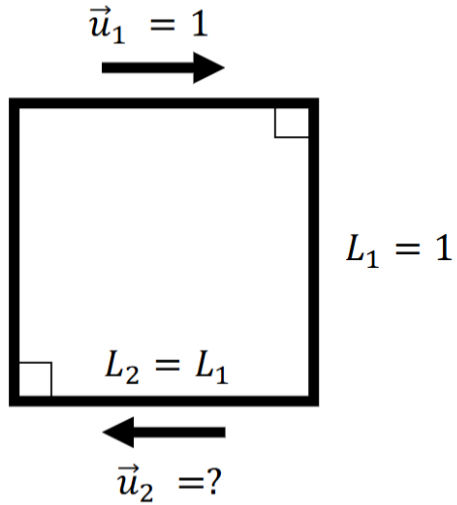


Figure 1: Cavity schematic with moving top and bottom walls

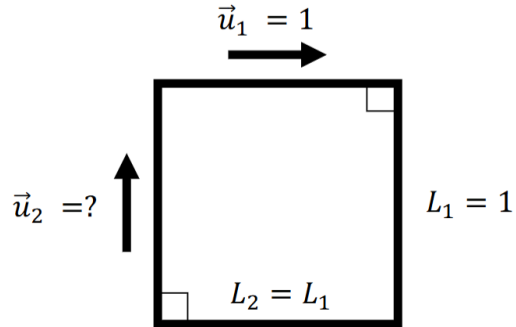


Figure 2: Cavity schematic with moving top and left walls

2.1 Governing Equations

The governing equations for 2D unsteady incompressible flow are the Navier-Stokes equations, written in dimensional form as:

$$\frac{\partial u}{\partial x} + \frac{\partial v}{\partial y} = 0 \quad (1)$$

$$\frac{\partial u}{\partial t} + u \frac{\partial u}{\partial x} + v \frac{\partial u}{\partial y} = -\frac{1}{\rho} \frac{\partial p}{\partial x} + \nu \left(\frac{\partial^2 u}{\partial x^2} + \frac{\partial^2 u}{\partial y^2} \right) \quad (2)$$

$$\frac{\partial v}{\partial t} + u \frac{\partial v}{\partial x} + v \frac{\partial v}{\partial y} = -\frac{1}{\rho} \frac{\partial p}{\partial y} + \nu \left(\frac{\partial^2 v}{\partial x^2} + \frac{\partial^2 v}{\partial y^2} \right) \quad (3)$$

To simplify the problem, the equations can be nondimensionalized using the characteristic length L which is the cavity side length and the velocity of the top plate U_0 . The nondimensional variables are:

$$x^* = \frac{x}{L}, \quad y^* = \frac{y}{L}, \quad u^* = \frac{u}{U_0}, \quad v^* = \frac{v}{U_0}, \quad t^* = \frac{tU_0}{L}, \quad p^* = \frac{p}{\rho U_0^2}$$

where the Reynolds number is defined as:

$$Re = \frac{U_0 L}{\nu}$$

Continuity Equation The continuity equation is described in Equation (1). Begin by substituting in the nondimensional variables.

$$\begin{aligned} \frac{\partial u}{\partial x} &= \frac{\partial(U_0 u^*)}{\partial(Lx^*)} = \frac{U_0}{L} \frac{\partial u^*}{\partial x^*}, \\ \frac{\partial v}{\partial y} &= \frac{\partial(U_0 v^*)}{\partial(Ly^*)} = \frac{U_0}{L} \frac{\partial v^*}{\partial y^*} \end{aligned}$$

So the continuity equation becomes:

$$\frac{U_0}{L} \left(\frac{\partial u^*}{\partial x^*} + \frac{\partial v^*}{\partial y^*} \right) = 0$$

Since $\frac{U_0}{L} \neq 0$, the continuity equation becomes nondimensionalized and written as:

$$\frac{\partial u^*}{\partial x^*} + \frac{\partial v^*}{\partial y^*} = 0 \quad (4)$$

X-Momentum Equation The dimensional x -momentum equation is described in Equation (2). By substituting the nondimensional variables:

$$\begin{aligned}\frac{\partial u}{\partial t} &= \frac{\partial(U_0 u^*)}{\partial(t^* L/U_0)} = \frac{U_0^2}{L} \frac{\partial u^*}{\partial t^*}, \\ u \frac{\partial u}{\partial x} &= U_0 u^* \cdot \frac{U_0}{L} \frac{\partial u^*}{\partial x^*} = \frac{U_0^2}{L} u^* \frac{\partial u^*}{\partial x^*}, \\ v \frac{\partial u}{\partial y} &= \frac{U_0^2}{L} v^* \frac{\partial u^*}{\partial y^*}, \\ \frac{1}{\rho} \frac{\partial p}{\partial x} &= \frac{1}{\rho} \cdot \frac{\partial(\rho U_0^2 p^*)}{\partial(Lx^*)} = \frac{U_0^2}{L} \frac{\partial p^*}{\partial x^*}, \\ \nu \frac{\partial^2 u}{\partial x^2} &= \nu \cdot \frac{U_0}{L^2} \frac{\partial^2 u^*}{\partial x^{*2}}, \quad \nu \frac{\partial^2 u}{\partial y^2} = \nu \cdot \frac{U_0}{L^2} \frac{\partial^2 u^*}{\partial y^{*2}}\end{aligned}$$

Putting all terms together:

$$\frac{U_0^2}{L} \left(\frac{\partial u^*}{\partial t^*} + u^* \frac{\partial u^*}{\partial x^*} + v^* \frac{\partial u^*}{\partial y^*} \right) = -\frac{U_0^2}{L} \frac{\partial p^*}{\partial x^*} + \nu \cdot \frac{U_0}{L^2} \left(\frac{\partial^2 u^*}{\partial x^{*2}} + \frac{\partial^2 u^*}{\partial y^{*2}} \right)$$

By dividing through by U_0^2/L , the nondimensional form of the x -momentum equation is obtained.

$$\frac{\partial u^*}{\partial t^*} + \frac{\partial(u^{*2})}{\partial x^*} + \frac{\partial(u^* v^*)}{\partial y^*} + \frac{\partial p^*}{\partial x^*} = \frac{1}{Re} \left(\frac{\partial^2 u^*}{\partial x^{*2}} + \frac{\partial^2 u^*}{\partial y^{*2}} \right) \quad (5)$$

Y-Momentum Equation Following a similar procedure the dimensional form of the y -momentum equation Equation (3) becomes nondimensionalized as:

$$\frac{\partial v^*}{\partial t^*} + \frac{\partial(v^{*2})}{\partial y^*} + \frac{\partial(u^* v^*)}{\partial x^*} + \frac{\partial p^*}{\partial y^*} = \frac{1}{Re} \left(\frac{\partial^2 v^*}{\partial x^{*2}} + \frac{\partial^2 v^*}{\partial y^{*2}} \right) \quad (6)$$

2.2 Initial and Boundary Conditions

Initially, the fluid is at rest.

$$u^*(x^*, y^*, 0) = 0, \quad v^*(x^*, y^*, 0) = 0$$

The nondimensional boundary conditions are defined for the first case as:

- Top wall ($y^* = 1$): $u^* = 1, v^* = 0$
- Bottom wall ($y^* = 0$): $u^* = -1, v^* = 0$
- Left and right walls ($x^* = 0$ and $x^* = 1$): $u^* = v^* = 0$

The nondimensional boundary conditions are defined for the second case as:

- Top wall ($y^* = 1$): $u^* = 1, v^* = 0$
- Left wall ($x^* = 0$): $u^* = 0, v^* = -1$
- Bottom and right walls ($y^* = 0$ and $x^* = 1$): $u^* = v^* = 0$

2.3 Assumptions

The following assumptions are made to simplify the model:

- The flow is two-dimensional and incompressible.
- The fluid is Newtonian with constant density and viscosity.
- The cavity is square, with side length L .
- No-slip boundary conditions are applied at all walls.

2.4 Analytical Solution

An exact analytical solution does not exist for the full unsteady Navier-Stokes equations in this geometry. The problem must be solved numerically.

3 Numerical Formulation

3.1 Marker and Cell (MAC) Method

3.1.1 Description of Staggered Grid and Storage Locations

The numerical solution of the transient lid-driven cavity problem utilizes the explicit Marker and Cell (MAC) method implemented upon a staggered grid. For this section of the paper, nondimensional quantities are referred to as x, y, u, v , etc. for the sake of readability when referencing intermediate quantities. The primary variables are staggered to improve numerical stability and ensure mass conservation. The horizontal velocity u is stored at the vertical cell faces, and the vertical velocity v is stored at the horizontal cell faces, and pressure p is calculated at the cell centers. This approach allows for the enforcement of the divergence-free condition of incompressible flow directly onto the grid. The velocity components at intermediate time steps are computed explicitly using central differencing for spatial derivatives and forward Euler integration for time-stepping. By discretizing the momentum equations, Equations (5) and (6), respectively,

$$\begin{aligned} u_{i+\frac{1}{2},j}^{n+1} &= u_{i+\frac{1}{2},j}^{*n} - \frac{\Delta t}{\Delta x} (p_{i+1,j}^{n+1} - p_{i,j}^{n+1}) \\ v_{i,j+\frac{1}{2}}^{n+1} &= v_{i,j+\frac{1}{2}}^{*n} - \frac{\Delta t}{\Delta y} (p_{i,j+1}^{n+1} - p_{i,j}^{n+1}) \end{aligned} \tag{7}$$

3.1.2 Equations for Intermediate Quantities

Intermediate velocities u^* and v^* are calculated explicitly with the forward Euler time-stepping scheme, using second-order central difference approximations for spatial derivatives.

$$u_{i+\frac{1}{2},j}^{*n} = u_{i+\frac{1}{2},j}^n + \Delta t \left[\frac{u_{i+\frac{3}{2},j} - 2u_{i+\frac{1}{2},j} + u_{i-\frac{1}{2},j}}{Re(\Delta x)^2} \right. \\ \left. + \frac{u_{i+\frac{1}{2},j-1} - 2u_{i+\frac{1}{2},j} + u_{i+\frac{1}{2},j+1}}{Re(\Delta y)^2} - \frac{u_{i+1,j}^2 - u_{i,j}^2}{\Delta x} \right. \\ \left. - \frac{(uv)_{i+\frac{1}{2},j+\frac{1}{2}} - (uv)_{i+\frac{1}{2},j-\frac{1}{2}}}{\Delta y} \right] \quad (8)$$

$$v_{i,j+\frac{1}{2}}^{*n} = v_{i,j+\frac{1}{2}}^n + \Delta t \left[\frac{v_{i+1,j+\frac{1}{2}} - 2v_{i,j+\frac{1}{2}} + v_{i-1,j+\frac{1}{2}}}{Re(\Delta x)^2} \right. \\ \left. + \frac{v_{i,j+\frac{3}{2}} - 2v_{i,j+\frac{1}{2}} + v_{i,j-\frac{1}{2}}}{Re(\Delta y)^2} - \frac{v_{i,j+1}^2 - v_{i,j}^2}{\Delta y} \right. \\ \left. - \frac{(uv)_{i+\frac{1}{2},j+\frac{1}{2}} - (uv)_{i-\frac{1}{2},j+\frac{1}{2}}}{\Delta x} \right] \quad (9)$$

with

$$u_{i+1,j} = \frac{1}{2}(u_{i+\frac{1}{2},j} + u_{i+\frac{3}{2},j}) \\ (uv)_{i+\frac{1}{2},j+\frac{1}{2}} = \left(\frac{u_{i+\frac{1}{2},j} + u_{i+\frac{1}{2},j+1}}{2} \right) \left(\frac{v_{i+1,j+\frac{1}{2}} + v_{i,j+\frac{1}{2}}}{2} \right)$$

3.1.3 Boundary Conditions

Boundary conditions are explicitly applied depending on the scenario. No-slip conditions are applied on walls that are stationary for any given case.

Antiparallel Top and Bottom-Driven Flow In this case, the top and bottom walls move with speed u_{wall} but in opposite directions, while the left and right walls are stationary.

- Top wall ($y = L$):

$$u_{y=L} = 2u_{\text{wall}} - u_{y=L-\Delta y}, \\ v_{y=L} = -v_{y=L-\Delta y}.$$

- Bottom wall ($y = 0$):

$$u_{y=0} = -2u_{\text{wall}} - u_{y=\Delta y}, \\ v_{y=0} = -v_{y=\Delta y}.$$

-
- Left and right walls ($x = 0$, $x = L$) (no-slip):

$$\begin{aligned} u_{x=0} &= -u_{x=\Delta x}, \\ u_{x=L} &= -u_{x=L-\Delta x}, \\ v_{x=0} &= -v_{x=\Delta x}, \\ v_{x=L} &= -v_{x=L-\Delta x}. \end{aligned}$$

Top and Left-Driven Flow In this case, the top and left walls move with speed u_{wall} , while the bottom and right walls are stationary.

- Top wall ($y = L$):

$$\begin{aligned} u_{y=L} &= 2u_{\text{wall}} - u_{y=L-\Delta y}, \\ v_{y=L} &= -v_{y=L-\Delta y}. \end{aligned}$$

- Bottom wall ($y = 0$) (no-slip):

$$\begin{aligned} u_{y=0} &= -u_{y=\Delta y}, \\ v_{y=0} &= -v_{y=\Delta y}. \end{aligned}$$

- Left wall ($x = 0$):

$$\begin{aligned} u_{x=0} &= -u_{x=\Delta x}, \\ v_{x=0} &= -2u_{\text{wall}} - v_{x=\Delta x}. \end{aligned}$$

- Right wall ($x = L$) (no-slip):

$$\begin{aligned} u_{x=L} &= -u_{x=L-\Delta x}, \\ v_{x=L} &= -v_{x=L-\Delta x}. \end{aligned}$$

3.2 Numerical Method for Poisson Solver

To enforce incompressibility in the flow, the pressure field p is obtained by solving the Poisson equation.

$$\nabla^2 p = f \tag{10}$$

on a unit square domain with homogeneous Dirichlet boundary conditions ($p = 0$ on all boundaries), where f is the source term derived from the divergence of the velocity predictor step.

3.2.1 Discretization

The domain is discretized on a uniform Cartesian grid with spacing h in both the x and y directions. A second-order central difference scheme is applied to approximate the Laplacian operator at interior points:

$$\frac{p_{i-1,j} - 2p_{i,j} + p_{i+1,j}}{h^2} + \frac{p_{i,j-1} - 2p_{i,j} + p_{i,j+1}}{h^2} = f_{i,j}. \tag{11}$$

This results in a sparse linear system of equations:

$$A\mathbf{p} = \mathbf{b}, \quad (12)$$

where \mathbf{p} is the vectorized pressure field at interior nodes.

3.2.2 Matrix Assembly

The coefficient matrix A is built using Kronecker products:

- A 1D Laplacian matrix T_{1D} with stencil $[-1, 2, -1]$ is constructed for each coordinate direction.
- The full 2D Laplacian matrix is assembled as:

$$A = I_N \otimes T_{1D} + T_{\text{off}} \otimes I_N, \quad (13)$$

where I_N is the $N \times N$ identity matrix, \otimes denotes the Kronecker product, and T_{off} introduces coupling between adjacent rows.

The right-hand side vector \mathbf{b} is constructed by scaling the source term f with h^2 and flattening it into a one-dimensional array.

3.2.3 Solution Method

The resulting sparse linear system is solved using a direct sparse solver (`spsolve` from SciPy). After solving for \mathbf{p} , the solution is reshaped back into a two-dimensional grid.

3.2.4 Summary of Steps

1. Discretize $\nabla^2 p = f$ using finite differences.
2. Assemble sparse matrix A via Kronecker products.
3. Flatten and scale the source term f .
4. Solve $A\mathbf{p} = \mathbf{b}$ using a sparse solver.
5. Reshape and shift the pressure field if necessary.

3.3 Code Sequence and Algorithm

The computational steps executed by the solver are as follows:

1. Initialize or update velocities based on boundary conditions.
2. Compute intermediate velocities explicitly using the MAC method.
3. Apply boundary conditions to intermediate velocities.

-
4. Compute divergence of intermediate velocities as the source term for the Poisson equation.
 5. Solve the Poisson equation for the pressure correction.
 6. Update velocities using the pressure gradient from the Poisson solution.
 7. Reapply velocity boundary conditions after the velocity update.
 8. Check for convergence based on relative velocity changes between iterations. Iterations continue until the error falls below the specified tolerance .

4 Results and Discussion

4.1 Validation of Numerical Solver using Top-Driven Flow

4.1.1 Mid-plane Velocity Profile

The accuracy of the numerical solver was validated against benchmark data from Mashayek [3]. The solver is initialized with $Re = 400$, $dt = 0.001$, $N = 100$ with boundary conditions for a top-driven lid flow, and no-slip conditions applied at the other three walls. Figure 3 shows that the computed results closely match the established benchmark solution, demonstrating the solver's accuracy.

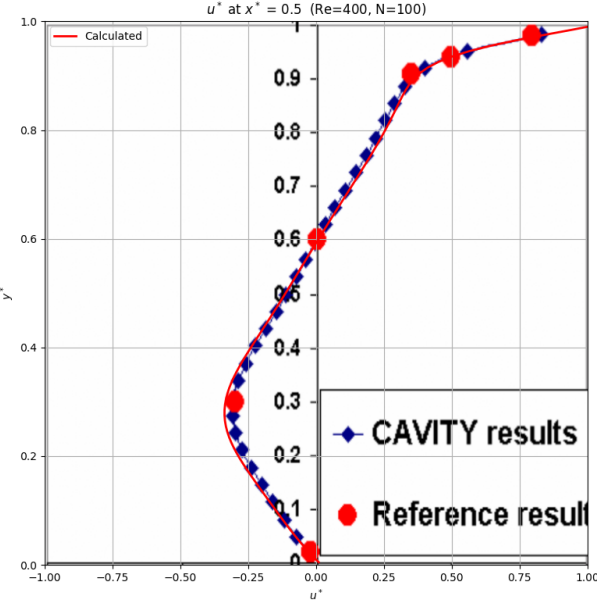


Figure 3: Comparison of Calculated and Benchmark Mid-Plane u^* -velocity for Top-Driven Flow at $Re = 400$.

4.1.2 Flow Field Visualization

The flow structures were further validated through visual inspection of streamline patterns and velocity vector fields, presented in Figures 4 and 5. These visualizations clearly capture the characteristic primary vortex near the cavity center, as well as secondary vortices located near the cavity corners, which align with the expected theoretical and numerical outcomes for this classic test case, Perumal and Dass [2].

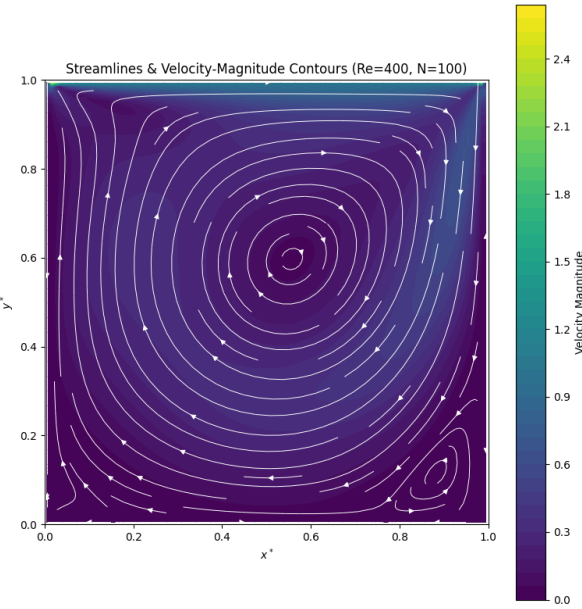


Figure 4: Streamlines and Velocity Magnitude Contours for Top-Driven Flow at $Re = 400$.

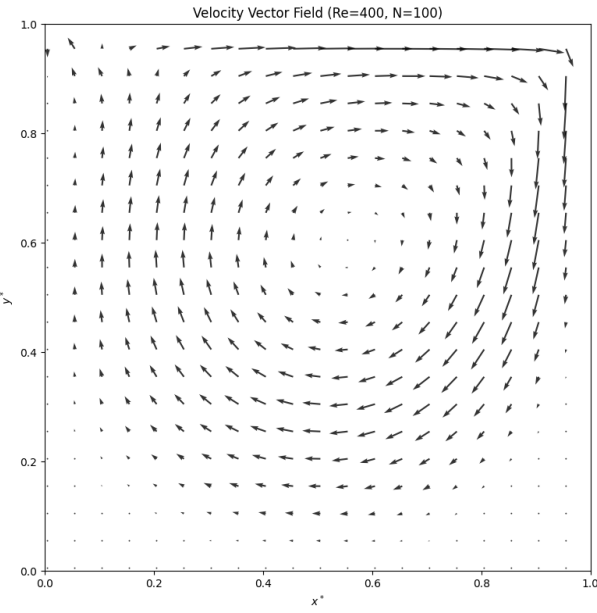


Figure 5: Velocity Vector Field for Top-Driven Flow at $Re = 400$.

These plots demonstrate a robust agreement with benchmark solutions, confirming that the implemented numerical solver reliably captures the main physical features of cavity-driven flows. Small discrepancies noted are within acceptable numerical error margins and can be further minimized by refining the computational grid or timestep.

4.2 Validation of Numerical Solver using Top and Bottom-Driven Antiparallel Flow

To further establish the accuracy of the numerical solver, a second validation study was conducted using top and bottom-driven antiparallel flow.

4.2.1 Mid-plane Velocity Profile

Using the data from Perumal and Dass [2], the mid-plane velocity profiles can be directly compared for $Re = 400$.

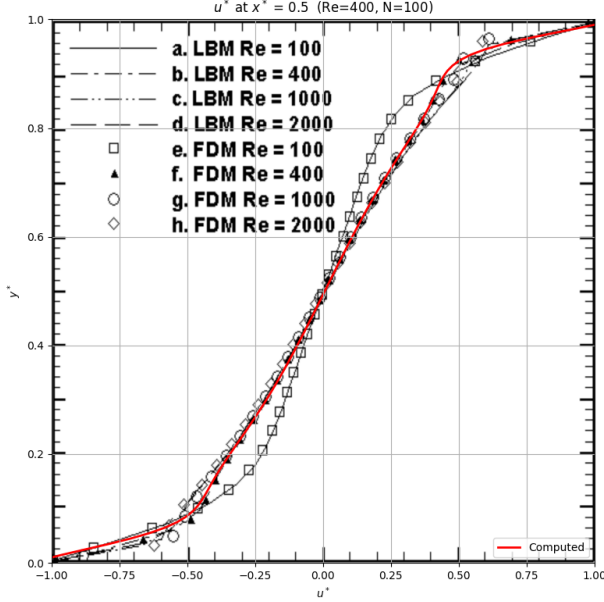


Figure 6: Mid-plane u^* -Velocity Profile for Antiparallel Flow at $Re = 400$.

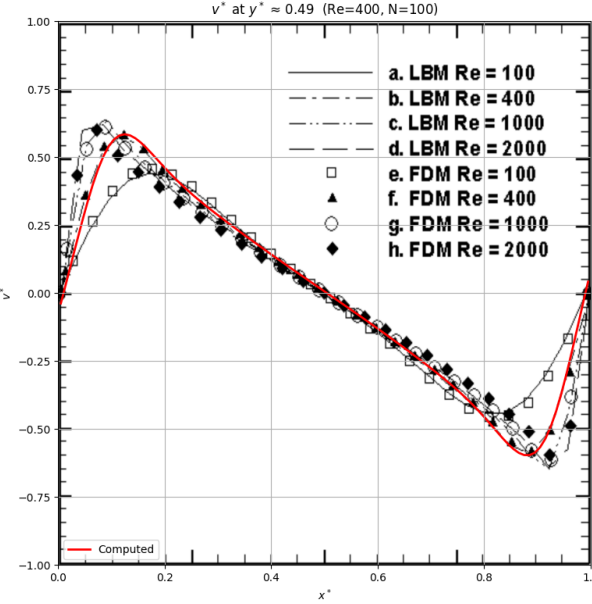


Figure 7: Mid-plane v^* -Velocity Profile for Antiparallel Flow at $Re = 400$.

Figures 6 and 7 clearly show that the calculated solution matches identically with the benchmark data, further demonstrating the solver's accuracy.

4.2.2 Flow Field Visualization

Visual inspection of the streamline and velocity vector fields compared to primary and secondary vortex locations as established by Perumal and Dass [2]. Figures 8 and 9 showcase vortices that closely align with the benchmark data, which has one large vortex in the center, and smaller vortices forming in opposite corners.

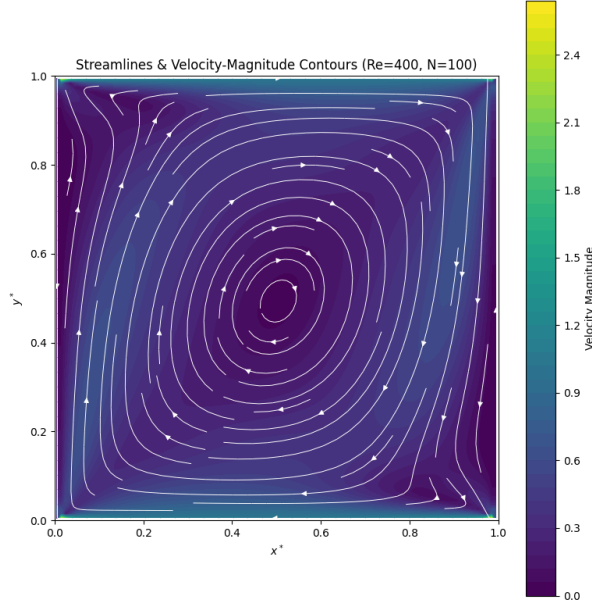


Figure 8: Streamlines and Velocity Magnitude Contours for Antiparallel Flow at $Re = 400$.

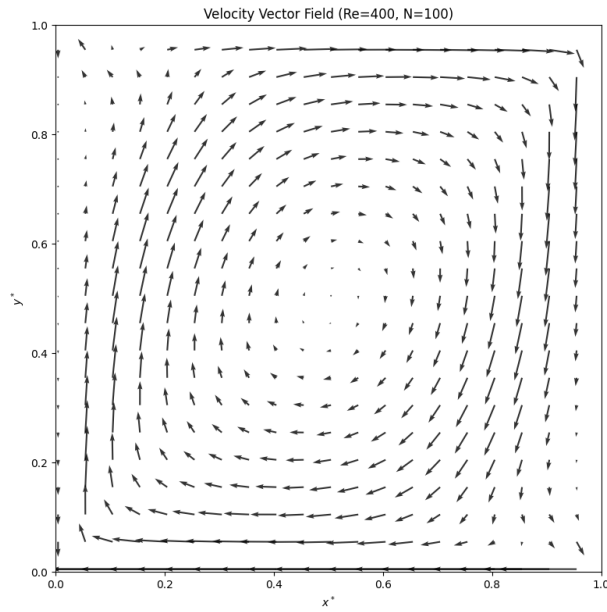


Figure 9: Velocity Vector Field for Antiparallel Flow at $Re = 400$.

4.3 Effects of Reynolds Number on Flow

4.3.1 Reynolds Study for Antiparallel Flow

The Reynolds number (Re) is a fundamental dimensionless parameter in fluid mechanics that characterizes the relative importance of inertial forces to viscous forces in a flow. In the lid-driven cavity problem, varying the Reynolds number allows us to systematically investigate

how the balance between these forces influences the flow structures inside the cavity. At low Reynolds numbers, viscous effects dominate, resulting in smooth, stable recirculating flows with thick boundary layers. As the Reynolds number increases, inertial effects become more significant, leading to the development of sharper velocity gradients, thinner boundary layers, stronger primary vortices, and the formation of secondary eddies near the corners. Studying the effect of Reynolds number thus provides critical insight into the transition from viscous-dominated to inertia-dominated flow regimes and serves as an important test of the numerical solver's ability to capture increasingly complex flow features. Figures 10-13 show the streamline patterns and velocity magnitude contours for $Re = 200, 400, 800$, and 1200 .

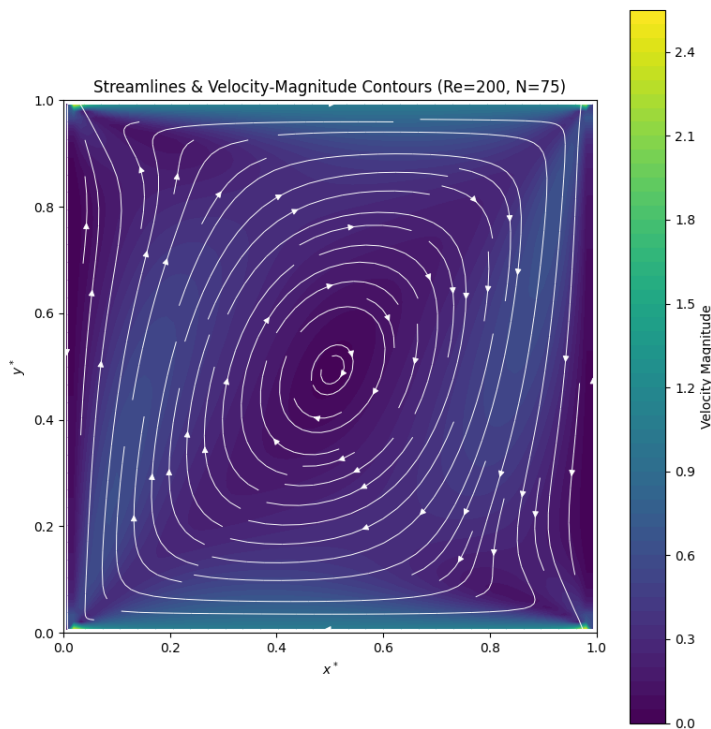


Figure 10: Streamlines and Velocity Magnitude Contours at $Re = 200$.

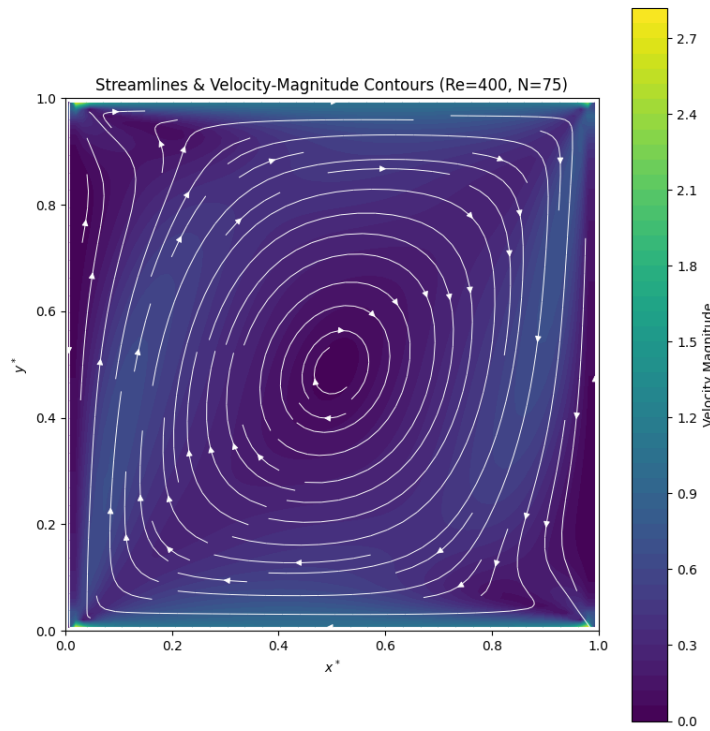


Figure 11: Streamlines and Velocity Magnitude Contours at $Re = 400$.

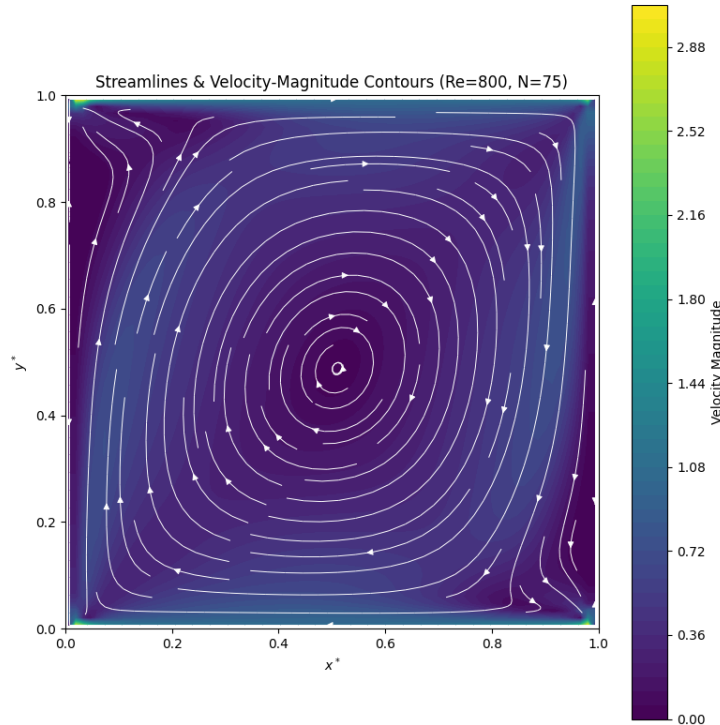


Figure 12: Streamlines and Velocity Magnitude Contours at $Re = 800$.

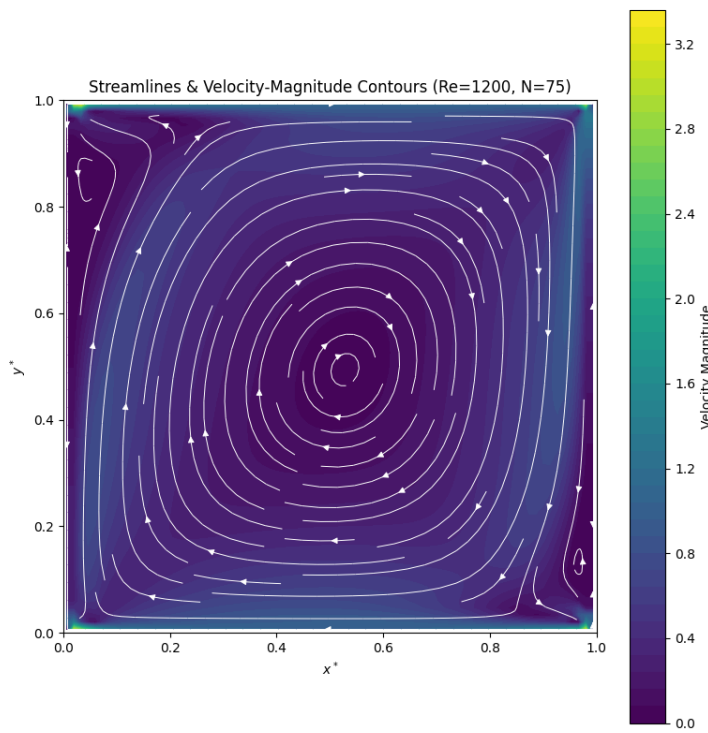


Figure 13: Streamlines and Velocity Magnitude Contours at $Re = 1200$.

Figures 14-17 present the corresponding velocity vector fields.

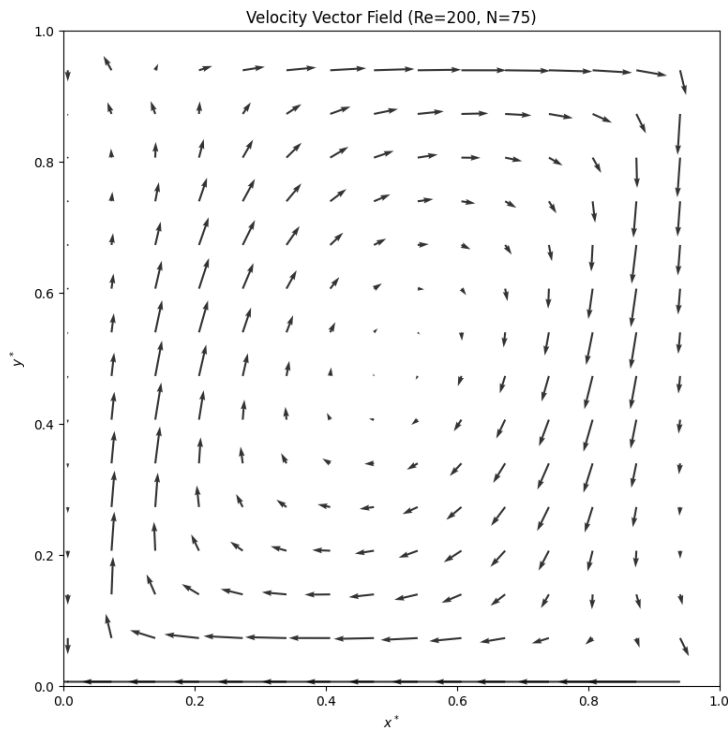


Figure 14: Velocity Vector Field at $Re = 200$.

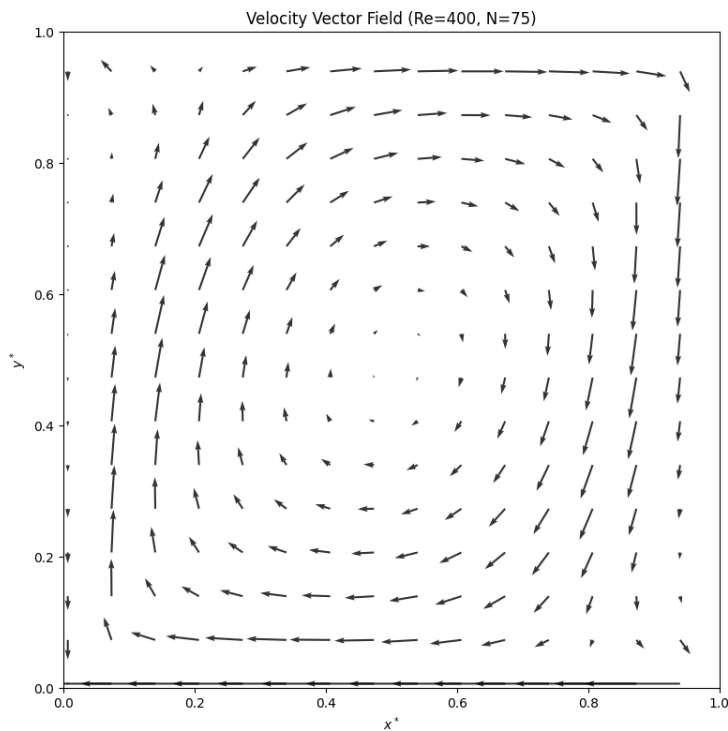


Figure 15: Velocity Vector Field at $Re = 400$.

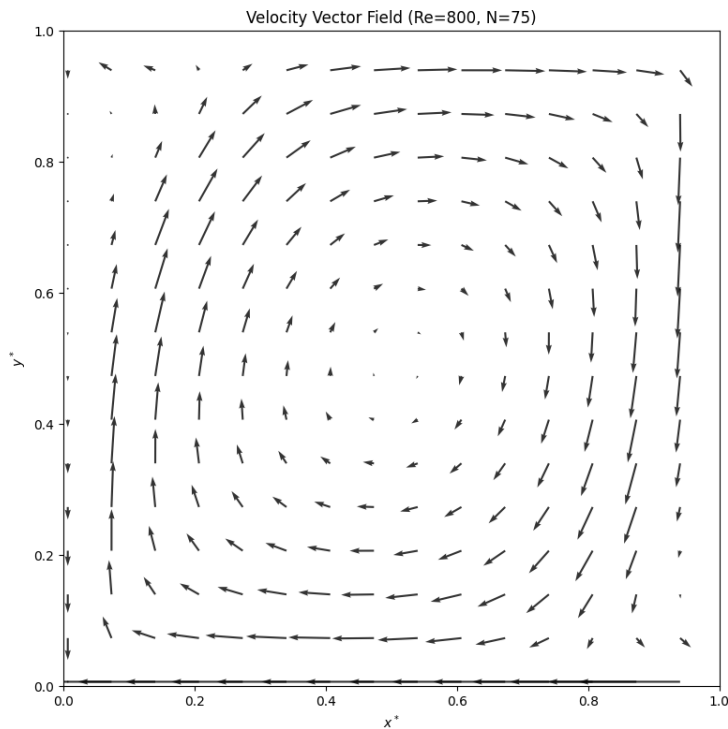


Figure 16: Velocity Vector Field at $Re = 800$.

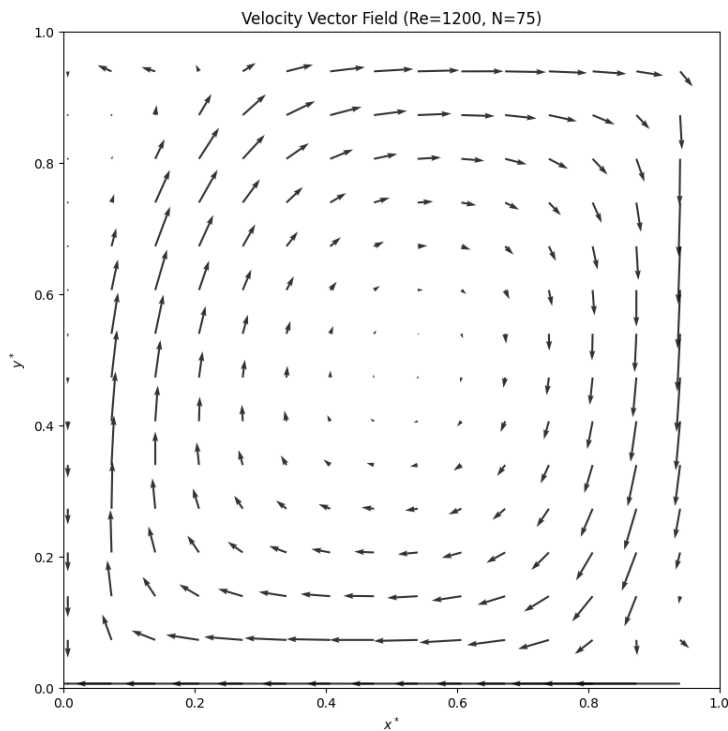


Figure 17: Velocity Vector Field at $Re = 1200$.

To further quantify the effect of Reynolds number, midplane velocity profiles are plotted. Figure 18 shows the u^* velocity at $x^* = 0.5$, and Figure 19 shows the v^* velocity at $y^* = 0.5$.

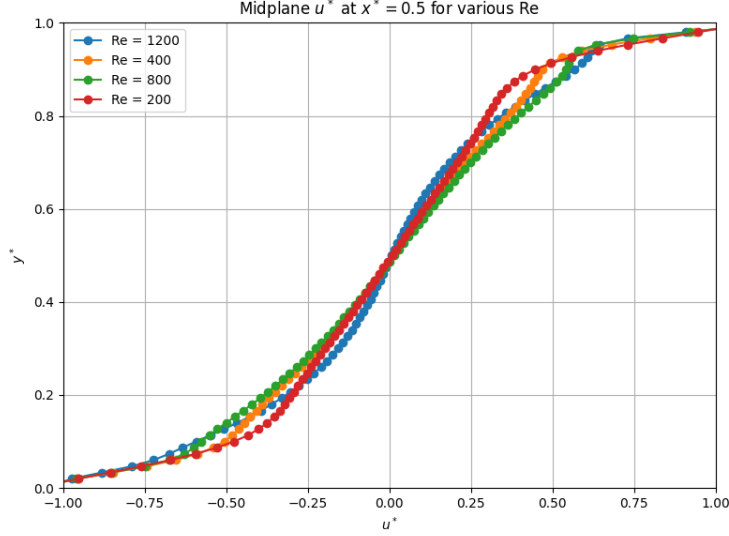


Figure 18: Mid-plane u^* Velocity Profiles at $x^* = 0.5$ for Different Reynolds Numbers.

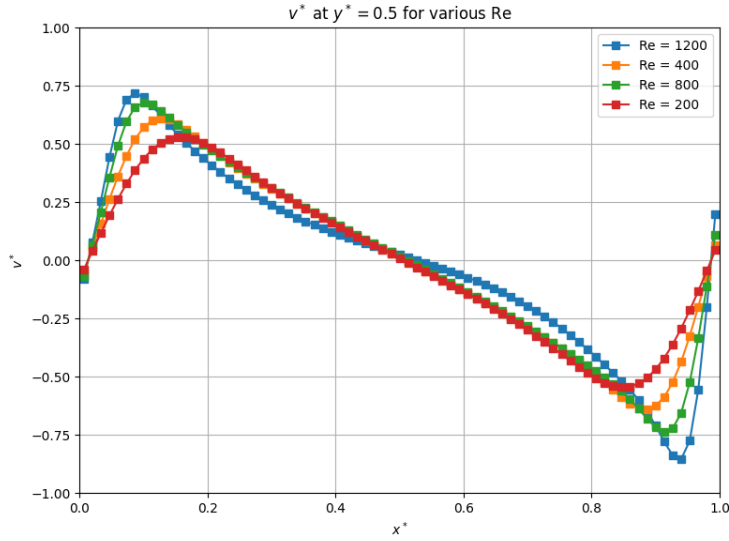


Figure 19: Mid-plane v^* Velocity Profiles at $y^* = 0.5$ for Different Reynolds Numbers.

The flow behavior inside the cavity shows a strong dependence on Reynolds number, as seen from the streamline patterns, velocity vector fields, and mid-plane velocity profiles:

- **Primary vortex behavior:** At lower Reynolds numbers (e.g., $Re = 200$), the primary vortex occupies most of the cavity, with a smooth and gradual recirculating flow. As the Reynolds number increases to $Re = 800$ and 1200 , the primary vortex becomes tighter, shifts closer to the center of the domain, and exhibits stronger rotation.

The strengthening of the primary vortex indicates a dominance of inertial effects over viscous damping.

- **Secondary vortex development:** Secondary corner vortices, which are absent at low Reynolds numbers, start to appear at $Re = 400$ and become clearly visible by $Re = 800$ and 1200. These secondary eddies form due to the interaction of the primary flow with the stationary walls, and their size and strength increase with Re . The presence of these vortices is a signature of more complex recirculating patterns and transition toward more inertial-dominated flow.
- **Boundary layer thinning:** As Re increases, the boundary layers along the moving walls (top and bottom) become noticeably thinner. In the contour plots, the regions of high velocity magnitude become confined to thin layers near the walls, while the interior flow remains relatively slower. This is consistent with classical fluid mechanics where higher Re leads to reduced viscous effects near walls, resulting in sharper velocity gradients.
- **Velocity magnitude increase:** The maximum velocity magnitude inside the domain increases with Reynolds number, especially near the moving walls. This is evident from the colorbars on the contour plots, which show a broader range of velocity values at higher Re .
- **Centerline velocity profiles:** The mid-plane u^* velocity profiles become flatter in the core region as Re increases, indicating that the flow in the center becomes more uniform at high Reynolds numbers. The profiles also become steeper near the walls, reflecting the thin boundary layer. The v^* velocity profiles at $y^* = 0.5$ exhibit higher peak values and sharper curvature near the center, consistent with enhanced secondary flow strength.
- **Symmetry considerations:** At all Reynolds numbers studied, the flow field remains symmetric about the vertical mid-plane ($x^* = 0.5$), as expected for this configuration. This symmetry serves as an internal validation of the numerical solver's stability and correctness.

Overall, these results clearly demonstrate the classic progression of cavity flow from viscous-dominated to inertia-dominated regimes as the Reynolds number increases. The solver successfully captures all expected qualitative behaviors, including vortex formation, boundary layer evolution, and increasing flow complexity at higher Re . The results of the Reynolds number study validate not only the physical realism of the simulated flows but also the numerical robustness of the developed solver. Across all Reynolds numbers considered, the solver consistently captures the essential features of lid-driven cavity flow, including vortex formation, boundary layer development, and secondary eddy generation. The observed trends match theoretical expectations and published benchmark results, confirming that the Marker and Cell (MAC) method combined with the developed pressure correction scheme provides an accurate and reliable tool for solving unsteady incompressible flows in confined geometries.

4.3.2 Reynolds Study for Corner Flow

When considering the case with the top and left walls moving, a Reynolds number study was conducted to investigate the evolving flow physics. The top wall moves rightward with nondimensional speed $u^* = 1$ and the left wall moves downward with nondimensional speed $v^* = -1$, while the bottom and right walls remain stationary. The grid resolution and timestep were kept constant across all Reynolds number cases. Figures 20–29 present the mid-plane velocity profiles, streamline patterns, and velocity vector fields for $Re = 200, 400, 600$, and 1000 .

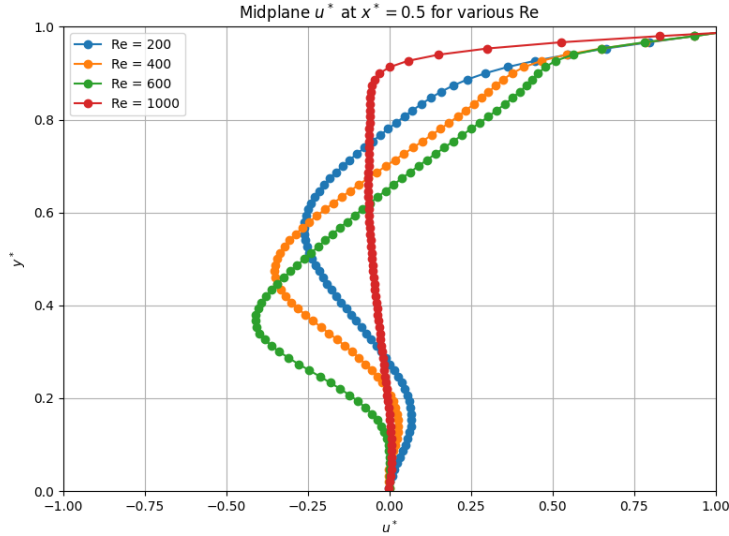


Figure 20: Mid-plane u^* velocity profiles at $x^* = 0.5$ for various Reynolds numbers (corner flow).

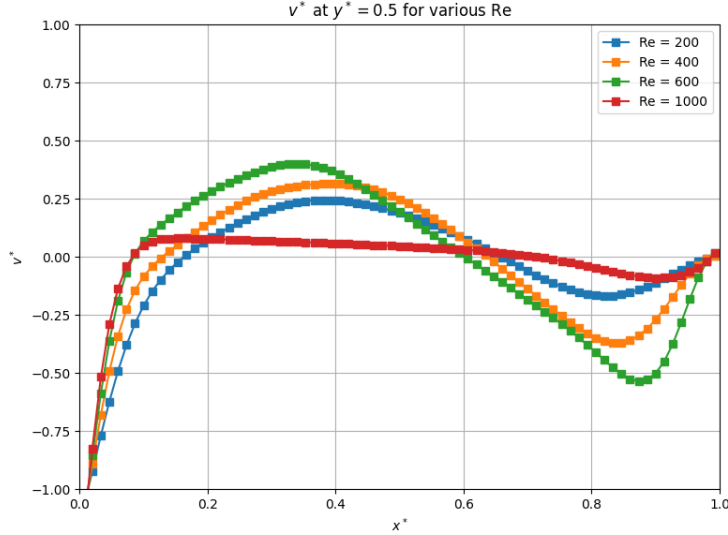


Figure 21: Mid-plane v^* Velocity Profiles at $y^* = 0.5$ for Various Reynolds Numbers (Corner Flow).

Key Observations:

- **Low Reynolds numbers (Re = 200):**
 - Flow is viscous dominated.
 - A primary vortex forms in the center, smooth and symmetric.
 - Velocity profiles are gradual, indicating thick boundary layers.
- **Moderate Reynolds numbers (Re = 400–600):**
 - Inertial effects strengthen.
 - The primary vortex tightens and shifts toward the moving walls.
 - Secondary vortices begin forming in the cavity corners.
 - Boundary layers near the top and left walls thin noticeably.
- **High Reynolds number (Re = 1000):**
 - Inertia-dominated flow with strong separation along bottom and right walls.
 - Multiple secondary eddies are well developed near the corners.
 - Velocity profiles show sharp gradients near walls and flattening in the core region.
 - Took longest to converge with the same grid and timestep

Physical Interpretation:

- As Reynolds number increases, viscous diffusion weakens relative to inertial transport, leading to sharper shear layers and more complex recirculation patterns.

- The interaction between the two moving walls (top and left) causes stronger swirling motion and more vigorous corner vortex development compared to single-wall driven flows.
- The thin high-speed layers along the top and left walls are signatures of boundary layer formation at high Re .

Overall, the results illustrate the classic transition from smooth, viscous-dominated flow to complex, inertia-driven multi-vortex flow as Reynolds number increases in a corner-driven cavity.

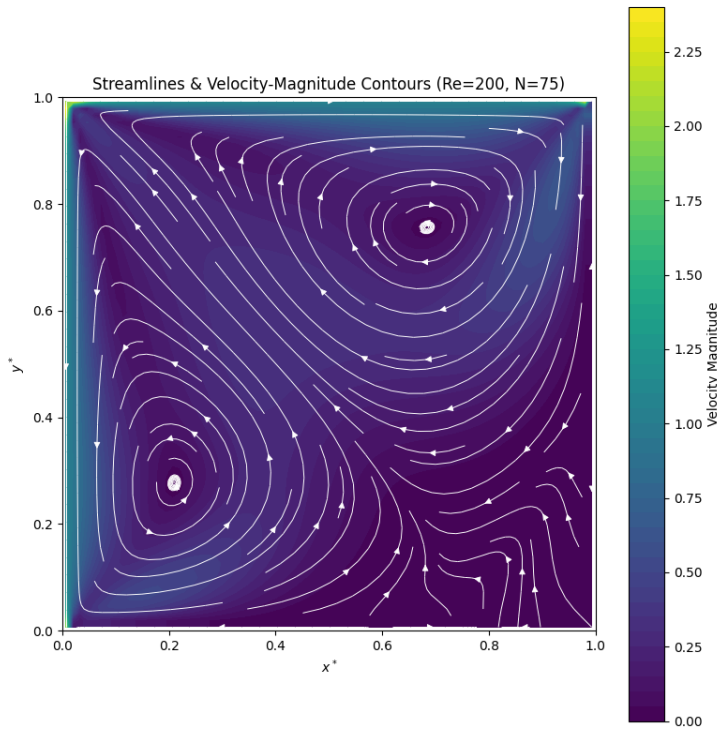


Figure 22: Streamlines and Velocity Magnitude Contours at $Re = 200$ (Corner Flow).

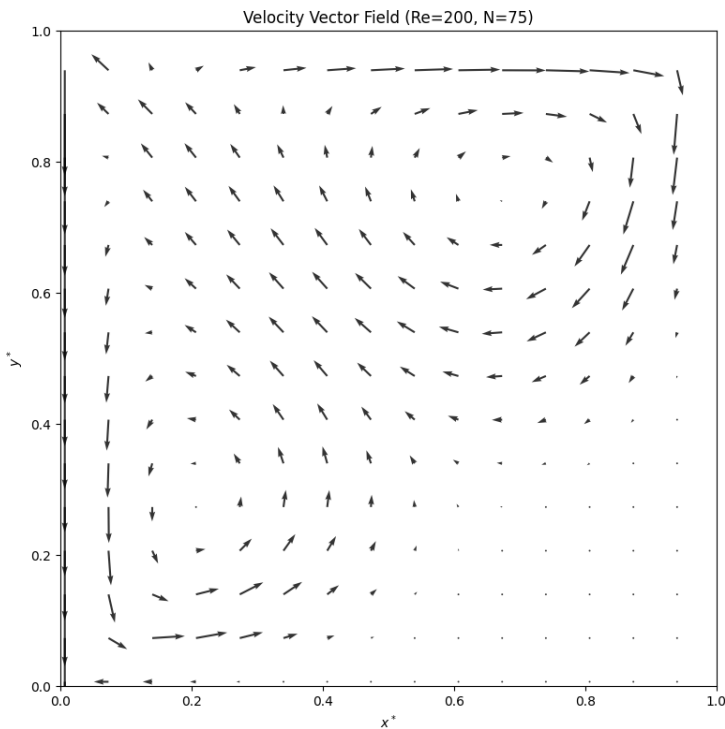


Figure 23: Velocity Vector Field at $Re = 200$ (Corner Flow).

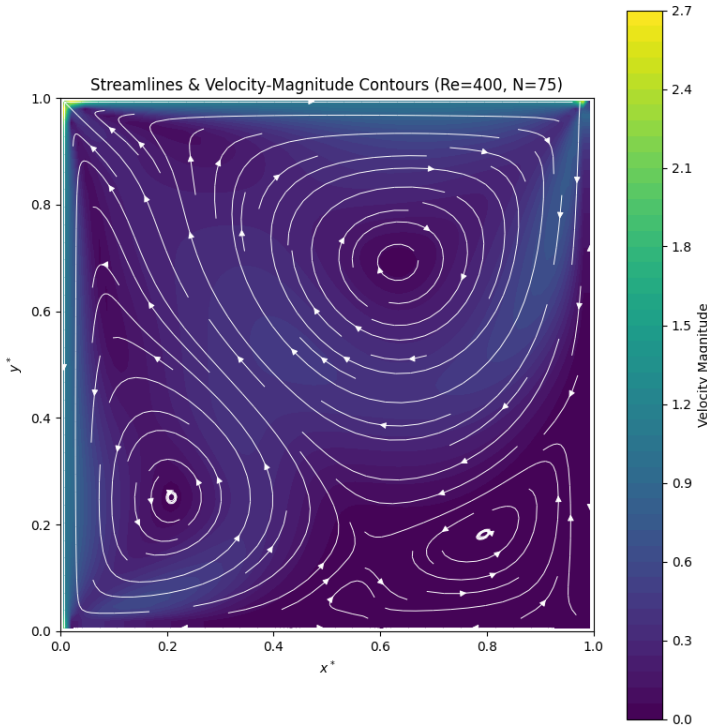


Figure 24: Streamlines and Velocity Magnitude Contours at $Re = 400$ (Corner Flow).

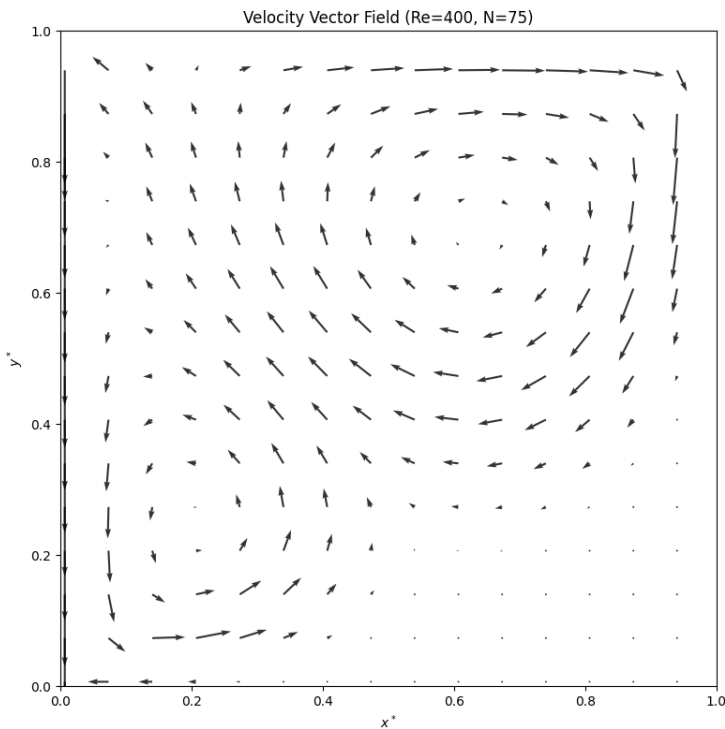


Figure 25: Velocity Vector Field at $Re = 400$ (Corner Flow).

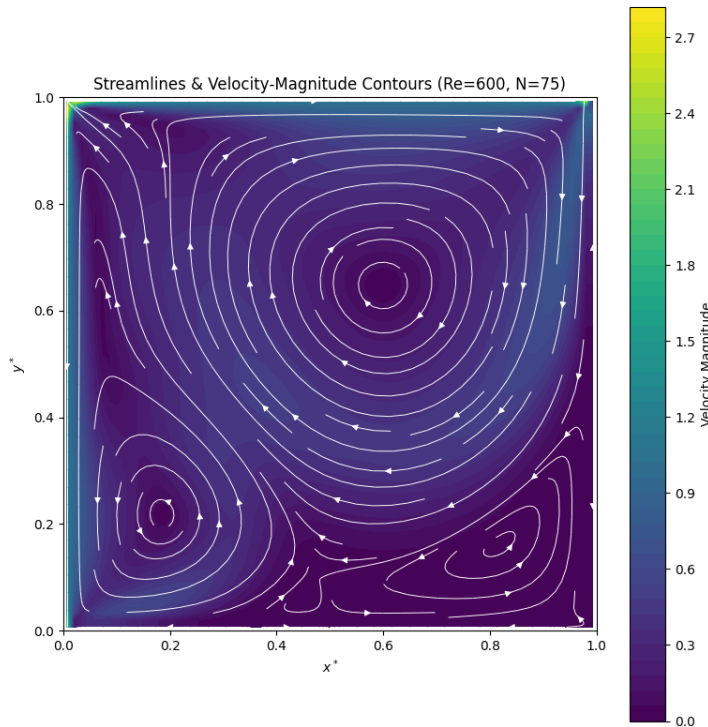


Figure 26: Streamlines and Velocity Magnitude Contours at $Re = 600$ (Corner Flow).

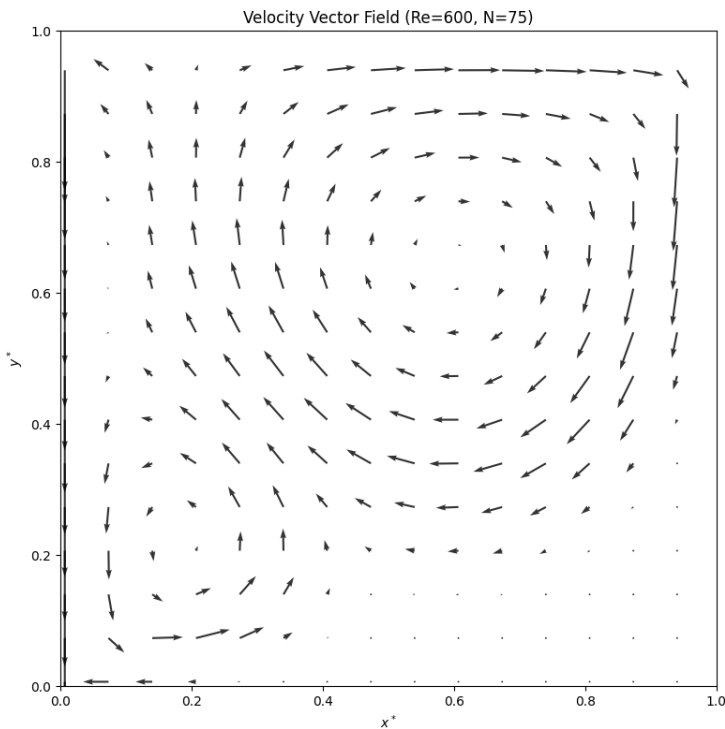


Figure 27: Velocity Vector Field at $Re = 600$ (Corner Flow).

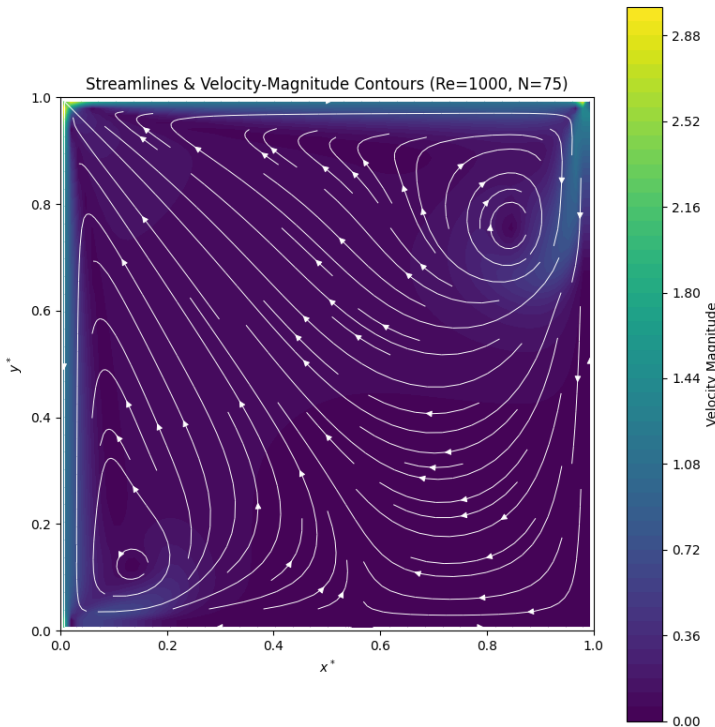


Figure 28: Streamlines and Velocity Magnitude Contours at $Re = 1000$ (Corner Flow).

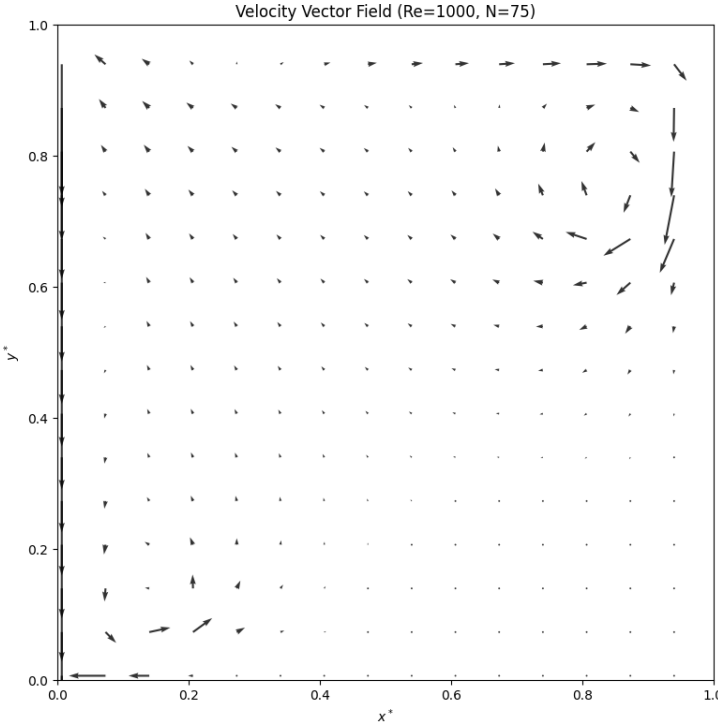


Figure 29: Velocity Vector Field at $Re = 1000$ (Corner Flow).

4.4 Effects of Δt on Flow

4.4.1 Time Study for Antiparallel Flow

To study the effects of timestep size on flow accuracy and stability, simulations were performed at Reynolds number $Re = 400$ using a 50×50 grid, simulated up to $t^* = 5$. A range of timestep sizes was explored: $\Delta t = 2 \times 10^{-2}, 1 \times 10^{-2}, 5 \times 10^{-3}, 1 \times 10^{-3}, 5 \times 10^{-4}, 1 \times 10^{-4}$, and 5×10^{-5} , where the smallest timestep served as the reference solution. Figure 30 presents a side-by-side comparison of streamline patterns for each timestep at $t^* = 5$. Across all timesteps tested, the streamline fields remained smooth and free of numerical oscillations. However, as Δt increases, the solution exhibits increasing deviation from the reference case. Specifically, the strength and shape of vortices become less accurate, with some loss of detail in secondary flow features. For $\Delta t \leq 5 \times 10^{-4}$, the streamlines are nearly indistinguishable from the reference.

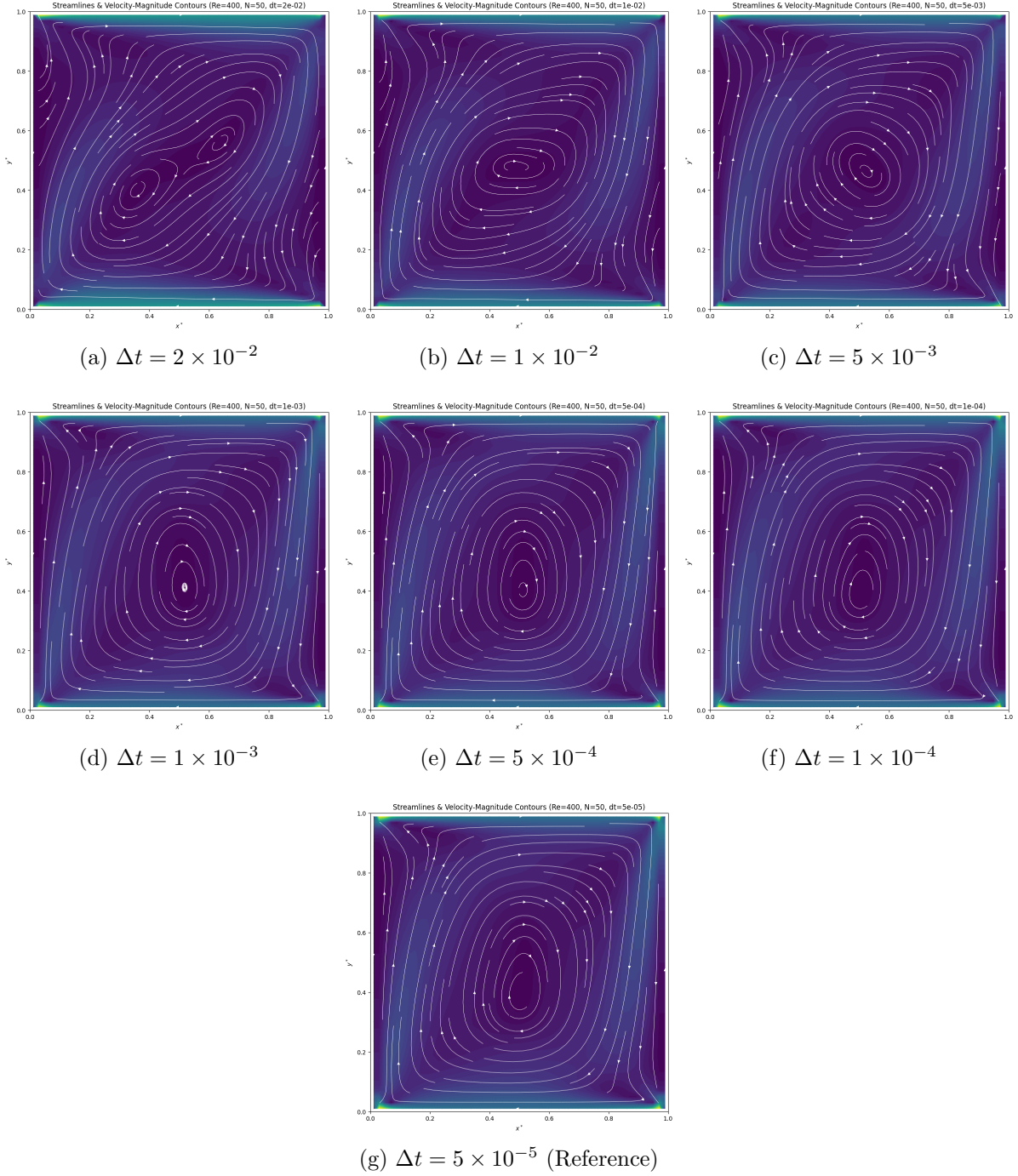


Figure 30: Streamlines and Velocity Magnitude Contours for various Δt at $t^* = 5$. Grid: 50×50 , $Re = 400$.

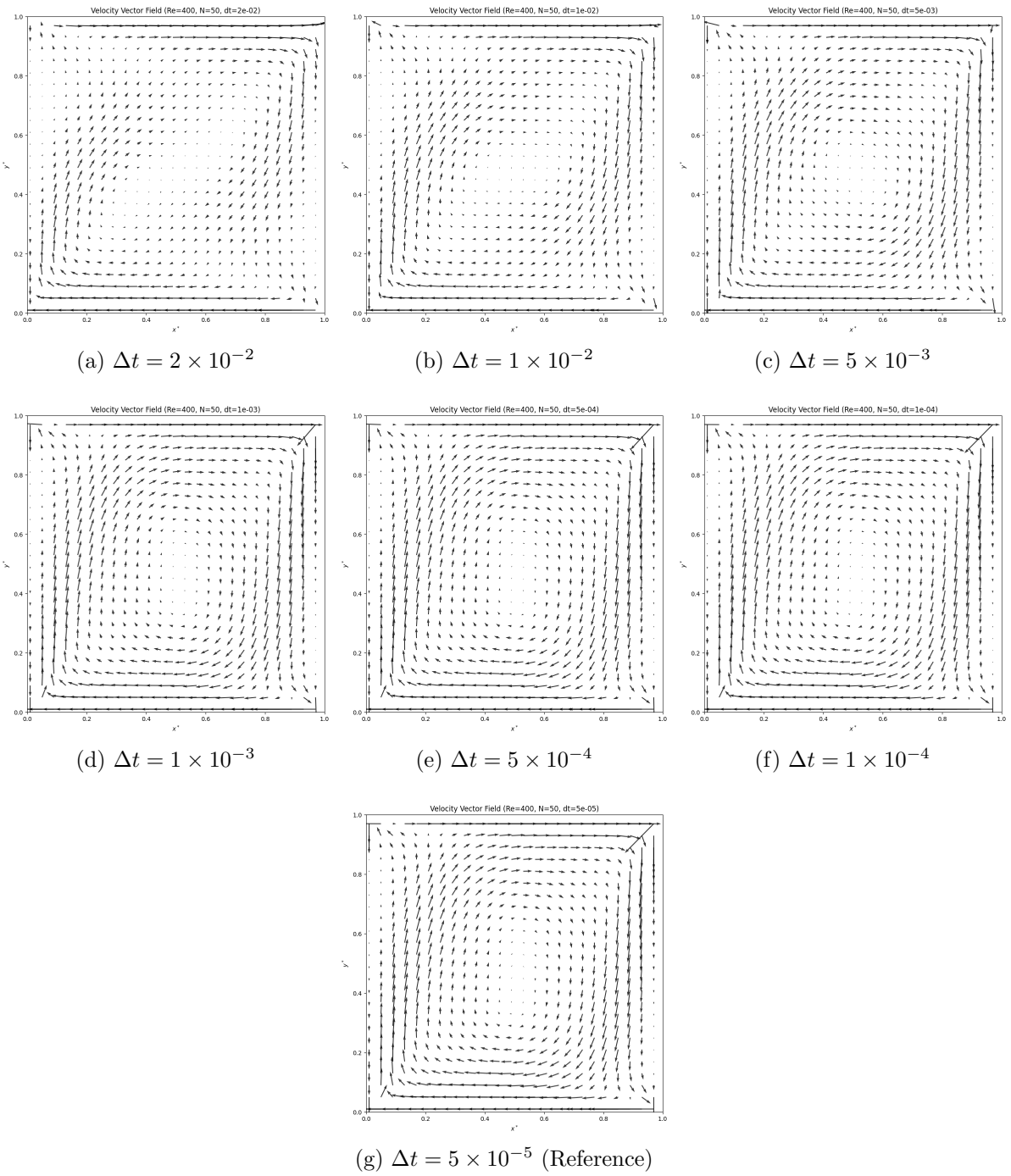


Figure 31: Velocity Vector Fields for Various Δt at $t^* = 5$. Grid: 50×50 , $Re = 400$.

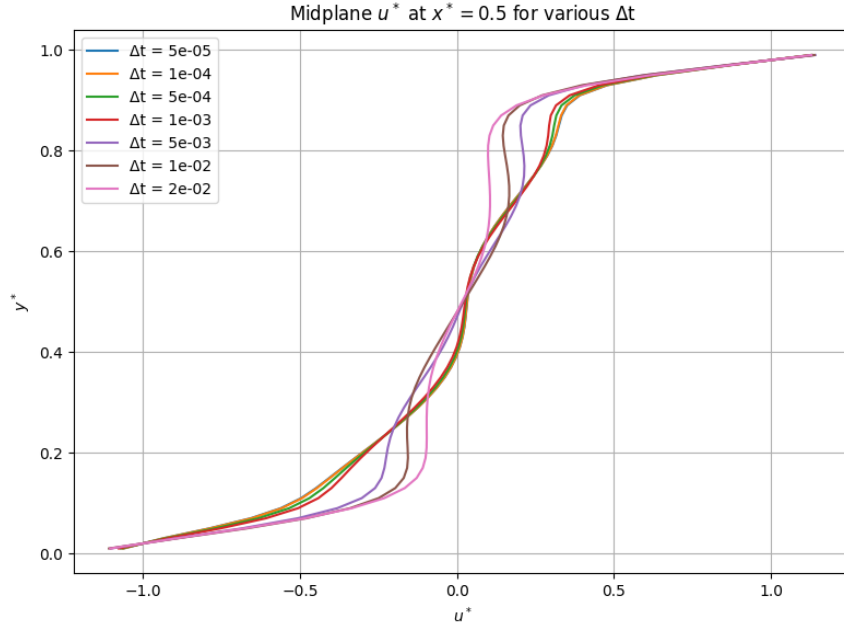


Figure 32: Mid-plane u^* Velocity Profiles at $x^* = 0.5$ for Various Δt .

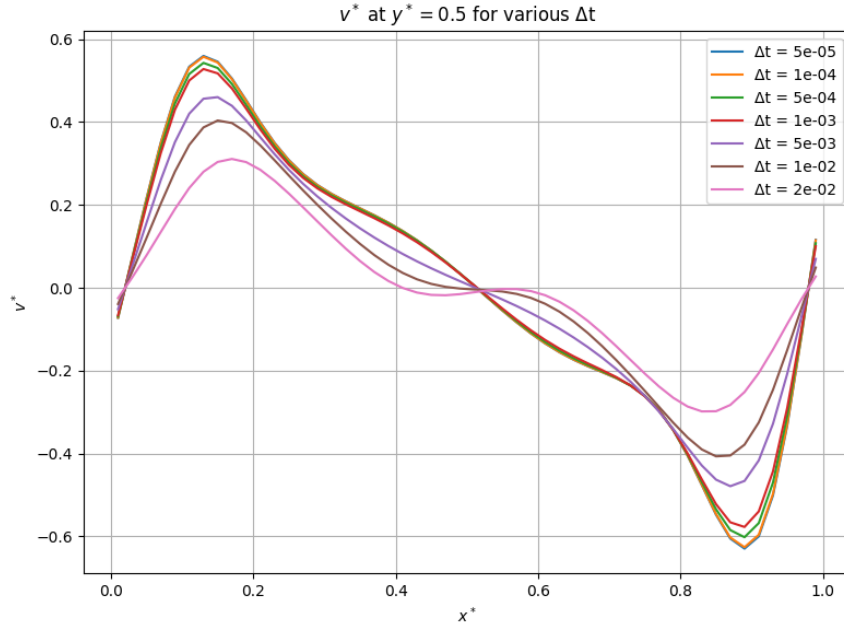


Figure 33: Mid-plane v^* Velocity Profiles at $y^* = 0.5$ for Various Δt .

4.4.2 Convective and Viscous Stability

The numerical stability of the explicit MAC method is governed by two nondimensional quantities: the convective Courant-Friedrichs-Lowy (CFL) number and the viscous von Neumann

number (VNN). The CFL number is defined as:

$$\text{CFL} = \frac{\Delta t}{\Delta x} \max(|u| + |v|)$$

and characterizes the stability of advective transport. For explicit schemes, numerical instability typically occurs when CFL exceeds 1. The viscous von Neumann number is defined as:

$$\text{VNN} = \frac{\Delta t}{Re(\Delta x)^2},$$

and describes the stability of diffusion terms. Although less restrictive than CFL, VNN must also remain small in explicit solvers.

Δt	Max CFL	VNN	L_2 Rel. Error
5×10^{-5}	0.0449	3.13×10^{-4}	0
1×10^{-4}	0.0897	6.25×10^{-4}	2.91×10^{-3}
5×10^{-4}	0.442	3.13×10^{-3}	2.59×10^{-2}
1×10^{-3}	0.870	6.25×10^{-3}	5.35×10^{-2}
5×10^{-3}	3.75	3.12×10^{-2}	2.01×10^{-1}
1×10^{-2}	6.10	6.25×10^{-2}	2.76×10^{-1}
2×10^{-2}	9.11	1.25×10^{-1}	3.23×10^{-1}

Table 1: Maximum CFL, VNN, and L_2 relative error for various Δt values.

Although the CFL number exceeds 1 for timestep sizes $\Delta t \geq 5 \times 10^{-3}$, no visible instabilities such as oscillations or divergence were observed in the streamline or velocity field plots. All solutions remained smooth and physically reasonable through $t^* = 5$. However, the L_2 error increases rapidly for larger Δt , and the flow structure deviates significantly from the reference solution. Any values for $\Delta t \geq 2 \times 10^{-2}$ causes divergence within the first 500 timesteps.

This deviation is attributed to under-resolution of the temporal evolution, not numerical instability. The VNN values remained small for all timesteps, indicating diffusion was not a limiting factor. Therefore, while the solver tolerated $\text{CFL} > 1$ in this configuration, temporal accuracy degraded. For reliable and accurate transient results, we recommend a timestep constraint:

$$\Delta t \leq 5 \times 10^{-4}$$

for $Re = 400$ on a 50×50 grid. Since the grid size would also affect the accuracy of the velocity values, CFL would change slightly with different grid sizes. VNN would vary with both different grid sizes and Reynolds number, as it is directly dependent.

4.5 Effects of $\Delta x, \Delta y$ on Flow

4.5.1 Space Study for Antiparallel Flow

To investigate the effects of spatial resolution on solution accuracy, a grid refinement study was conducted for the antiparallel lid-driven cavity flow at $Re = 400$. Simulations were

performed using uniform grids with $N = 25, 50, 75, 100$, and 150 points in each direction, while maintaining a constant timestep size ($\Delta t = 0.001$) and final simulation time ($t^* = 5$). Figures 34 and 35 show the mid-plane u^* and v^* velocity profiles for each grid. As grid resolution increases, the computed profiles converge toward smooth curves, and fluctuations diminish significantly. Coarser grids like $N = 25$ exhibit noticeable numerical diffusion, under-resolving peak velocities and boundary layer gradients, whereas finer grids such as $N = 100$ and $N = 150$ closely reproduce the established velocity profiles reported by Perumal and Dass [2].

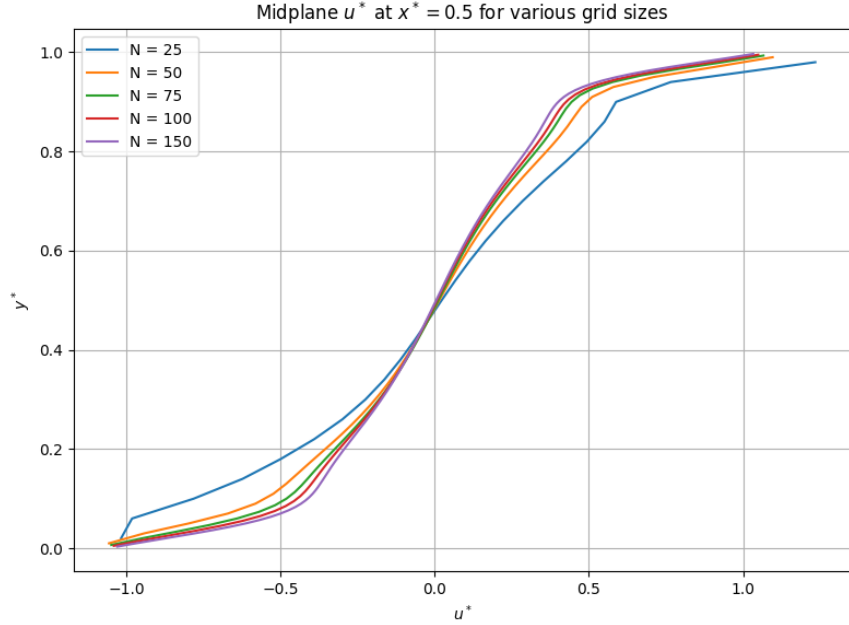


Figure 34: Mid-plane u^* Profiles at $x^* = 0.5$ for Various Grid Sizes

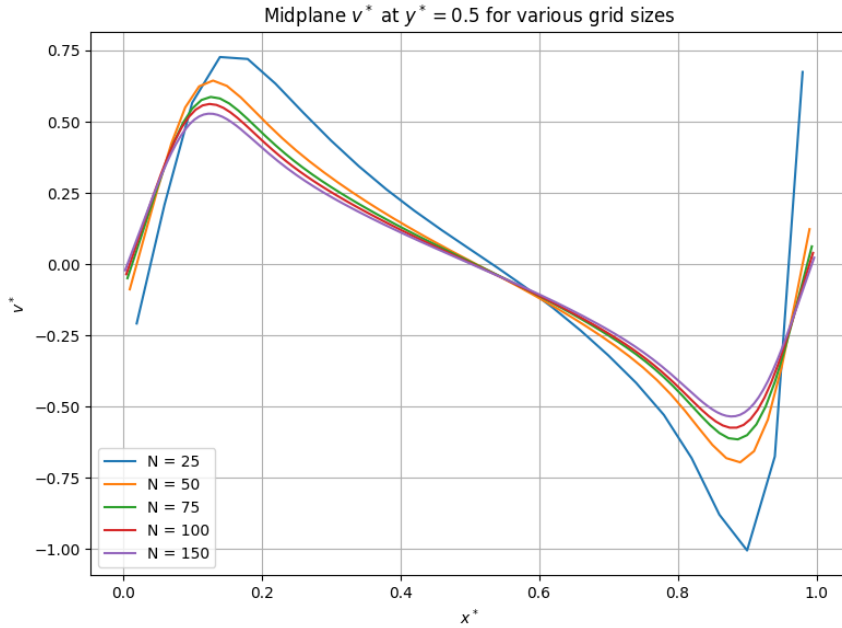


Figure 35: Mid-plane v^* Profiles at $y^* = 0.5$ for Various Grid Sizes

Key Observations:

- **Coarse grids ($N = 25$):** The primary vortex is resolved, but secondary corner vortices are poorly captured. Velocity profiles show under-prediction of peak velocities and excessive smoothing of boundary layers.
- **Intermediate grids ($N = 50$ and $N = 75$):** Flow structures and velocity profiles improve markedly. Secondary vortices begin forming, and boundary layers thin appreciably.
- **Fine grids ($N = 100$ and $N = 150$):** Full resolution of primary and secondary vortices is achieved. Velocity gradients near the walls become sharper, and mid-plane velocity profiles match closely with benchmark solutions from Perumal and Dass [2].

Physical Interpretation:

- Increased grid resolution reduces numerical diffusion, better capturing the steep velocity gradients in the boundary layers and the finer structures of secondary corner vortices.
- Coarse grids suppress flow features by artificially smearing inertial effects, particularly evident in flattened mid-plane velocity profiles and weaker vortices.
- Finer grids allow for improved resolution of inertial and viscous force balances, enabling better agreement with established CFD benchmarks.

Conclusion from Grid Study:

-
- A minimum grid size of $N = 75$ to $N = 100$ is recommended to accurately capture the primary and secondary flow features at $Re = 400$.
 - The profiles at $N = 100$ and $N = 150$ exhibit excellent agreement with the published benchmark results of Perumal and Dass [2], validating the accuracy of the MAC solver developed in this study.
 - Although a finer grid ($N = 150$) marginally improves flow detail, it significantly increases computational cost. Thus, $N = 100$ offers a practical balance between accuracy and efficiency for this study.
 - Due to time and hardware limitations, even finer grids such as $N = 200$ were not feasible within project constraints. However, the observed convergence trend strongly suggests continued improvement with grid refinement.

5 Conclusion

This study investigated the unsteady incompressible flow inside a square lid-driven cavity using the Marker and Cell (MAC) method on a staggered grid. Two primary flow configurations were considered: antiparallel flow driven by opposing top and bottom walls, and corner flow driven by orthogonal top and left walls. The Navier-Stokes equations were nondimensionalized and discretized using forward Euler time-stepping and central differencing in space. Pressure was solved using a Poisson equation with Dirichlet boundary conditions. The solver was validated against benchmark data for both top-driven and antiparallel cavity flows, and further tested through parametric studies in Reynolds number, timestep size, and grid resolution.

The results confirmed that the MAC solver reliably captures key flow structures such as primary and secondary vortices, boundary layers, and symmetric velocity profiles. The Reynolds number study showed a clear transition from viscous to inertia-dominated regimes, with sharper gradients, thinner boundary layers, and increasing secondary vortex strength as Re increased. Timestep size directly impacted temporal accuracy: large Δt values introduced significant deviation from the reference solution but remained stable up to a point. Grid refinement revealed that a resolution of $N = 100$ balances accuracy with computational cost; lower resolutions under-predict key features, while finer grids like $N = 150$ provide minimal gains for high cost. The solver was also validated through Poisson test problems with less than 0.5% error.

Future work could explore more complex variations of the cavity flow problem. One extension would be to vary the velocities of the two moving walls to analyze asymmetric interactions and shear layer development. Additionally, stretched or non-uniform grids could be introduced to better resolve thin boundary layers without excessive computation. Further analysis of the corner-driven flow case at higher Reynolds numbers would provide deeper insight into vortex dynamics and instability onset. Finally, other wall motion combinations—such as diagonal or rotating lids—could be studied to simulate more advanced flow scenarios and test solver generality.

References

- [1] U. Ghia, K. N. Ghia, and C. T. Shin, “High-Re Solutions for Incompressible Flow Using the Navier-Stokes Equations and a Multigrid Method,” *Journal of Computational Physics*, vol. 48, no. 3, pp. 387–411, Dec. 1982, doi: [https://doi.org/10.1016/0021-9991\(82\)90058-4](https://doi.org/10.1016/0021-9991(82)90058-4).
- [2] D. A. Perumal and A. K. Dass, “Simulation of flow in two-sided lid-driven square cavities by the lattice Boltzmann method,” *WIT Transactions on Engineering Sciences*, May 2008, doi: 10.2495/afm080051.
- [3] F. Mashayek, “Cavity Validation Data,” d2l.arizona.edu, 2025. <https://d2l.arizona.edu/d2l/le/content/1549961/viewContent/18560007/View> (accessed Apr. 26, 2025).
- [4] J. H. Ferziger and M. Peric, *Computational Methods for Fluid Dynamics*, Springer, 2001.

A Poisson’s Equation Solver Validation

Poisson’s Equation is used to solve for a pressure correction and ensure that velocity does not diverge. A validation test case of the numerical solver is contained in this appendix. The objective is to use the Poisson solver as discussed in Section 3.2 with a constant source term g , and visualize the resulting temperature distribution.

$$\nabla^2 T = \frac{\partial^2 T}{\partial x^2} + \frac{\partial^2 T}{\partial y^2} = -g \quad (14)$$

Consider the Poisson equation in two dimensions on a square domain $[0, L_x], [0, L_y]$, with Dirichlet boundary conditions $T = 1$ on all sides. The solution represents a steady-state temperature field driven by a uniform internal heat source. $\Delta = \Delta x = \Delta y$ is utilized for a uniform grid. The test case uses the parameters $N_x = N_y = 21$ and $g = 100$.

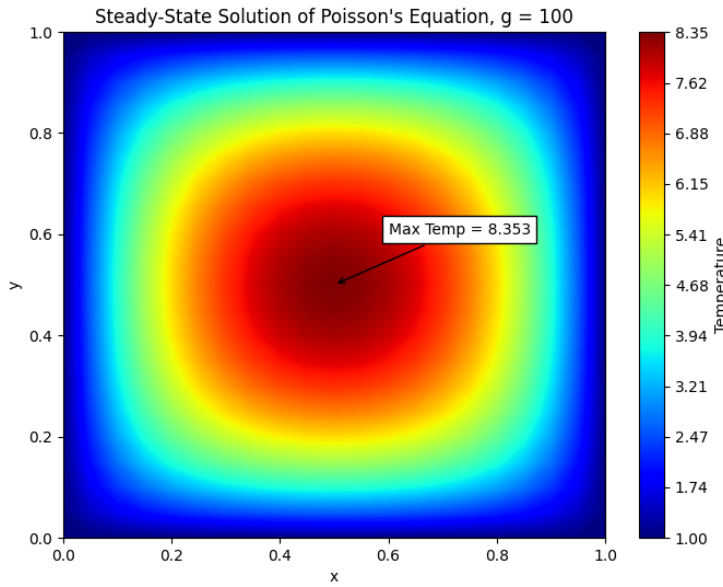


Figure 36: Poisson Validation Results

The max temperature at the center point was calculated to be 8.353. This is compared to the established results for the same parameters.

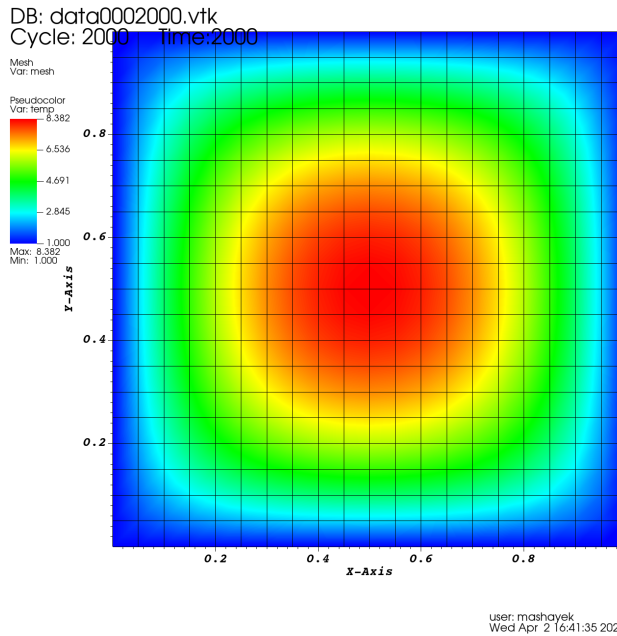


Figure 37: Poisson Established Results

The max temperature at the center point for the established results was calculated to be 8.382. The percent difference between the two results is 0.35%. This difference is acceptable, and thus the Poisson solver developed for this project is valid.